Passive Acoustic Dynamic Differentiation and Mapping (PADAM): A Time-Domain Passive Cavitation Localization and Classification Approach

Nathan Caso, *Graduate Student Member, IEEE*, Krunal Patel, and Tao Sun, *Member, IEEE*

Abstract*—*Objective: **Passive cavitation imaging has explored various beamforming algorithms to optimize spatial resolution, suppress imaging artifacts, and maintain computational efficiency. These factors are crucial for the clinical translation of Focused Ultrasound (FUS) therapies, where precise cavitation localization and dose control are required to minimize off-target effects. Commonly used methods such as Delay-Sum-Integrate (DSI) and Robust Capon Beamforming (RCB) have shown utility, but are limited by either significant artifacts or the need for a non-physical input parameter. To address these challenges, we aimed to develop a method that enhances resolution and introduces a physically grounded parameter for signal characterization, without compromising computational speed and robustness. *Methods:* This work introduces Passive Acoustic Dynamic Differentiation and Mapping (PADAM), which adapts the Multiple Signal Classification algorithm to the time domain to improve cavitation localization and classification. PADAM incorporates a physically meaningful input parameter that dynamically reflects the frequency richness of the received signal. *Results:* PADAM achieves up to a 6-fold improvement in lateral beamwidth compared to RCB, and a 4-fold reduction in mean-square artifact intensity reduction. Its input parameter provides a novel physical insight, enabling differentiation between stable and inertial cavitation based on spectral content. This reduces reliance on empirically tuned or arbitrary thresholds and simplifies integration into therapy workflows. *Conclusion:* With its ability to improve resolution, reduce artifacts, and provide computational efficiency, PADAM represents a promising advancement for precise cavitation localization and therapy monitoring. *Significance:* This work introduces PADAM, a time-domain passive cavitation imaging method that offers superior resolution and artifact reduction compared to DSI and RCB. Its physically intuitive input parameter enables dynamic differentiation between stable and inertial cavitation, enhancing precision in the monitoring and control of FUS therapy.**

***Index Terms*—Adaptive beamformers, cavitation imaging, passive cavitation mapping, ultrasound beamforming, focused ultrasound.**

I. INTRODUCTION

PASSIVE cavitation imaging (PCI) has gained significant attention for its role in monitoring cavitation-facilitated therapeutic applications, including targeted drug delivery, focal ablation, and others. These therapeutic applications often utilize a focused ultrasound (FUS) transducer to induce acoustic cavitation—with or without the introduction of preseeded bubbles—enabling spatially precise biological effects. For example, bubble cavitation can promote the controlled release and delivery of therapeutics, allowing treatment to access otherwise inaccessible regions, such as across the blood-brain barrier. Both preclinical and clinical studies have demonstrated enhanced therapeutic efficacy when cavitation-based approaches are applied to conditions such as Alzheimer's disease, glioblastoma, and other pathologies [3], [4], [5], [6], [7], [8], [9].

However, the stronger mode of cavitation, commonly referred to as inertial cavitation, can be destructive at high FUS pressures, causing either undesired or desired damage and cell death due to mechanical stress and hyperthermia [5], [10]. Non-invasive control and monitoring of cavitation-facilitated FUS therapy remain as a key challenge, traditionally addressed using MRI-based techniques or PCI, the latter being more cost-effective and time efficient [11], [12], [13]. PCI (Fig. 1) uses a passive listening device to estimate cavitation power and localize the treatment, making it a topic of significant interest in array signal processing [14]. High-resolution beamforming algorithms are crucial for improving the clinical viability of this passive imaging. Conventional approaches, such as Delay-Sum Integrate (DSI) and the Robust Capon Beamformer (RCB), have been used for cavitation power estimation and localization, and each display inherent trade-offs in resolution, speed, and artifact suppression [14], [15], [16], [17], [18], [19].

Received 28 May 2025; revised 25 July 2025; accepted 29 July 2025. Date of publication 7 August 2025; date of current version 15 January 2026. This work was supported by the Institute for Chemical Imaging of Living Systems of Northeastern University, Northeastern University College of Engineering, and the National Institute of General Medical Sciences of the National Institutes of Health under Award R35GM160097. *(Corresponding author: Tao Sun.)*

Nathan Caso and Krunal Patel are with the Department of Bioengineering, Northeastern University, USA.

Tao Sun is with the Department of Bioengineering, Northeastern University, Boston, MA 02115 USA, and also with the Institute for Chemical Imaging of Living Systems, Northeastern University, Boston, MA 02115 USA (e-mail: t.sun@northeastern.edu).

This article has supplementary downloadable material available at https://doi.org/10.1109/TBME.2025.3596596, provided by the authors.

Digital Object Identifier 10.1109/TBME.2025.3596596

Classical Passive Beamforming Techniques: The Delay-And-Sum (DAS) beamformer remains a commonly used method due to its computational efficiency [15], [16], [17], [18]. DAS estimates pixel intensity by summing delayed signals from multiple transducer channels based on their respective distances to the pixel location [20]. A subsequent variant, Delay-Sum Integrate (DSI), extends DAS to cases where the incoming wavefront time is not known, or there are many wavefronts to consider. By integrating across all available time indices, DSI provides a long-exposure-like reconstruction of cavitation events [21]. DSI may be implemented in either the time or frequency domain, with accuracy and speed improvements achieved by selecting frequencies associated with stable or inertial cavitation [22]. Although DSI is well-suited for real-time applications due to its computational efficiency [23], [24], [25], [26], it suffers from comparatively poor resolution and a characteristic tail artifact, a nonphysical effect resulting from the overlapping wavefront delays across channels.

To mitigate these limitations, adaptive beamformers have been explored, notably the Capon beamformer (CBs) and their enhanced version that prevent self-nulling, the Robust Capon Beamformer (RCB) [14], [19], [23]. Several studies have shown that RCB improves localization accuracy compared to DSI, aligning well with measured bio-effects in vitro [22]. However, despite its advantages in resolution, RCB is computationally intensive and requires tuning a steering vector uncertainty parameter, ε [14]. This parameter, defined as:

$$||a(\theta_0) - a(\theta_0 + \Delta)||^2 \leq \varepsilon \tag{1}$$

Quantifies the allowable uncertainty in the steering vector $a(\theta)$ [27]. Selecting an optimal ε is done once for an imaging application; however, the parameter has no tangible meaning in the context of cavitation physics. Some works suggest tuning it to around 8.45 [19], but it can be of arbitrary order of magnitude for a given application, field of view, or source location among other factors. Eigenspace-based RCB has been proposed to reduce the variance of the input parameter [28], but ε remains an empirically determined factor rather than a physically measurable parameter.

Multiple Signal Classification (MUSIC) is established in far-field array sensing (such as radar and sonar applications) for high-resolution and high signal to noise ratio (SNR) direction-finding. It is a frequency-domain direction-of-arrival beamformer that uses eigenvalue analysis assuming the presence of m scatterers [29]. The incoming signal is assumed to be modeled as the summation of discrete sinusoidal sources and noise, which is divisible into two orthogonal subspaces: the signal subspace and the noise subspace, and linear algebra is used to separate the two. MUSIC was explored by Polichetti et al. [30] for PCI, wherein the authors noted the beamformer's ability to distinguish low-intensity sources with a trial-error estimate of the parameter m. The computational study noted that a single bubble source contributed more than one eigenvector to the signal subspace in some cases, opening the question of the physical meaning of the MUSIC parameter in the context of PCI.

Proposed PADAM Approach: Cavitation emissions from multiple bubble sources are generated with the same drive frequency, and the stochastic time variances involved are on smaller scales than the sampling rates involved in passive imaging. Thus, the signals will clearly be correlated, and the MUSIC parameter m would not correspond to the exact number of sources in the incoming signal, consistent with the observations in Polichetti et al. [30]. Instead, we theorize that broadband signals present in inertial cavitation represent a signal subspace that is uncorrelated with the harmonic and ultraharmonic signals associated with stable cavitation, and that for a signal containing both inertial and stable cavitation emission, there is a value of m for that can separate the two phenomena.

To explore the role of the parameter m and address the limitations of existing beamforming approaches, we introduce a time-domain adaptation of the MUSIC direction-finding algorithm to the field of PCI. We refer to this method as Passive Acoustic Dynamic Differentiation and Mapping (PADAM), emphasizing its unique ability to dynamically classify the spectral richness of acoustic emissions. PADAM leverages time-domain MUSIC to overcome the trade-offs commonly encountered in existing beamformers—namely, between resolution, computational speed, and artifact suppression. It also offers a physically grounded interpretation of the m parameter by exploiting its capacity to distinguish frequency signatures based on the rank characteristics of the incoming signal's spatial covariance matrix.

The remainder of this work is organized as follows: Section II is a Methodology that includes 1) a derivation of the PADAM signal model, 2) an explanation of MUSIC in the frequency domain, 3) a derivation of MUSIC in the time-domain, 4) an explanation of the computational models used, 5) an explanation of the experimental methods used, and 6) an explanation of the metrics used to compare the beamformers. Section III (Results) presents findings from both in-silico and in-vitro experiments, analyzed using the aforementioned metrics. Section IV (Discussion) compares PADAM's capabilities and limitations against DSI and RCB. Section V (Conclusion) summarizes key findings and suggests directions for future research.

II. METHODS

PADAM Signal Model: The original MUSIC is a frequency domain direction-of-arrival beamformer that uses eigenvalue analysis and assumes the presence of m uncorrelated scatterers [29]. It divides the received radio frequency (RF) data into a noise and signal subspace, and assumes the incoming signal can be modeled as the summation of discrete sinusoidal sources and noise:

$$x_{(M\times k)} = A_{(M\times D)} s_{(D\times k)} + n_{(M\times k)} \tag{2}$$

Here, A as the matrix of steering vectors corresponding to M channels with D actual sources, s is the signal vector for a snapshot with k samples, and n is the noise vector. For convenience, we will use $k = 1$ for the remainder of the signal model. Next, we define the spatial covariance matrix R_{xx} as the expected value of the sample covariance matrix:

$$R_{xx} = E\{xx^H\} = AR_sA^H + \sigma^2 I \tag{3}$$

Where the signal covariance matrix $R_s = E\{ss^H\}$ is of size $D \times D$, and the spatial covariance matrix is of size $M \times M$. To satisfy the assumption that $R_{xx} = E\{xx^H\}$, multiple snapshots are often used:

$$R_{xx} = \frac{1}{N}\sum_{k=1}^{N_s} xx^H \tag{4}$$

Because $R_{xx} = AR_sA^H + \sigma^2 I$, the rank of R_s is equal to the number of sources D, and the rank of the noise matrix $\sigma^2 I$ is zero, the rank of $R_x x$ is also D. This means that there are D nonzero eigenvalues of R_{xx} corresponding to the signal, and $M - D$ near-zero eigenvalues corresponding to noise. The eigenvalue decomposition of R_{xx} is:

$$R_{xx} = V\Lambda V^{-1} \tag{5}$$

Where $\Lambda = \sum_{i=1}^{M} \lambda_i I_{ii}$ and λ_i is the i'th eigenvalue, and V is a matrix of the eigenvectors, sorted in the order of the largest to smallest eigenvalues.

Classical MUSIC Reconstruction: With the signal model established, reconstruction using MUSIC proceeds as follows: The incoming signal is either accumulated or divided into "snapshots", $x_{(n_t \times n_c)_i}$, which are averaged in the frequency-domain. n_t is the number of time samples, and n_c is the number of transducer channels, so x is a matrix with n_t rows and n_c columns. The spatial covariance matrix estimate is also generated during this step by taking the inner product:

$$\hat{X}_{(n_c,n_c)} = \frac{1}{n_s}\sum_{i=0}^{n_s} X_i^* X_i \tag{6}$$

Where n_s is the number of snapshots used. Note that X_i is the frequency-domain representation of the i'th snapshot, requiring a Fourier transform. Next, the eigenvalue decomposition of the averaged spatial covariance matrix estimate is computed:

$$\hat{X} = V\Lambda V^{-1} \tag{7}$$

From this decomposition, the number m of scatterers is selected by the user, assuming the signal rank D of $\hat{X}$ The m largest eigenvalues are selected from the decomposition, where $m < M$.

$$\lambda_1, \lambda_2, \ldots \lambda_m \in \Lambda \tag{8}$$

The associated eigenvectors from each of these m eigenvalues form the signal subspace, $V_s \in (M \times m)$, and the remaining $n_c - m + 1$ eigenvectors form the noise subspace, $V_n \in (M \times M - m)$. For each direction (or pixel location in the near-field), the pseudo-spectral intensity is calculated as the inverted inner product of the steered noise subspace:

$$P_{MUSIC}(\phi) = \frac{1}{A(\phi)V_n V_n^* A(\phi)^*} \tag{9}$$

With $A(\phi)$ as the steering vector. Notably, from this derivation, MUSIC does not yield a power estimate. It is instead inversely proportional to the noise power; when the noise subspace is orthogonal and uncorrelated (i.e., the signal subspace is highly correlated), then the MUSIC pseudo-spectrum is large.

PADAM - MUSIC Time-Domain: In this work, we adapt the MUSIC algorithm for the time-domain to form the PADAM algorithm. The input signal $x_{(n_t,n_c)}$ is delayed in time according to the geometric distance between each transducer's position $p(x, y)$ and a pixel location $a(x, y)$, using the one-way time of flight at the speed of sound, following the DSI approach:

$$\tilde{x}_{(n_t - n_{hyp}, n_c)} = x\left(\vec{t}_{hyp} + \frac{|p(\vec{i}) + a(\vec{i})|}{c \times dt}, i\right) \tag{10}$$

Where i is the index of a channel or transducer. The delays may be computed using a circular shift including all samples, or n_{hyp} samples corresponding to the hyperbola shape of the delay across channels may be omitted, as done in this work, and indicated by $\vec{t}_{hyp}$ in (10).

Next, the delayed signal is treated as $n_t - n_{hyp}$ snapshots in time, and averaged in the time-domain:

$$\hat{x} = \sum_{i=0}^{n_t - n_{hyp}} x_i^T x_i \tag{11}$$

As in the frequency-domain approach, the eigen-analysis is performed, but in this case, the entire decomposition is real-valued:

$$\hat{x} = V\Lambda V^{-1} \tag{12}$$

The pixel value is calculated from the noise subspace as before, but because a delay has already been applied, the subspace inner product is no longer steered during this step. Specifically, the steering vector $A(\phi)$ is replaced with a vector of ones, which is equivalent to the two-dimensional summation of the matrix elements:

$$P_{MUSIC}(x, y) = \frac{1}{\sum\sum V_n V_n^T} \tag{13}$$

The algorithm is laid out step-by-step in Algorithm 1.

In comparison to classical MUSIC, our PADAM time-domain approach offers the advantage of more extensive snapshot averaging, at the sacrifice of a potentially expensive average calculation recalculating the eigenvalue decomposition for each pixel. One significant advantage of this time-domain method is its simplicity. The frequency domain method requires careful management of snapshot lengths to retain relevant frequency information when splitting a frame of RF data into snapshots. Moreover, the time-domain method eliminates the need for windowing, overlapping, and dividing the signal into deliberate snapshots, offering a more straightforward approach without sacrificing essential data integrity.

Computational Bubble Model: Vokurka's bubble signal model provides a computational framework for simulating the time-series behavior of cavitating microbubbles using stochastic distributions. This model offers a unique platform for testing beamformer performance, as the location of a bubble source can be arbitrarily controlled in both space and time. The model is based on Vokurka's observations on cavitation behavior, where a cavitation event can be modeled over time by the equation [31],

```
Algorithm 1: PADAM Time-Domain.
Input: Delay matrix $\mathbf{D}_{(\mathbf{n_x \times n_y \times n_s})}$ containing the
       delays in units of indices at the sample rate for
       the one-way time of flight from each pixel in
       the lateral $(n_x)$ and axial $(n_y)$ directions to
       each transducer element $(n_s)$, Signal matrix
       $\mathbf{S}_{(\mathbf{n_t \times n_s})}$, with the raw RF data for $n_t$ time
       points and the $n_s$ transducer elements, Number
       of PADAM assumed sources, $\mathbf{m}$
Output: Beamformed Image $\mathbf{B}_{(\mathbf{n_x \times n_y})}$
S_{(n_t × n_s)} ← RF data
for $i \leftarrow 1$ to $n_x, j \leftarrow 1$ to $n_y$ do
    for $k \leftarrow 1$ to $n_s$ do
        $S \leftarrow circshift(S, D_{i,j,k})$
    $\mathbf{R}_{(\mathbf{n_s \times n_s})} \leftarrow$ zeros
    for $n \leftarrow 1$ to $n_t$ do
        $R = R + S_n S_n^T$
    $V \Lambda V^{-1} \leftarrow eig(R)$
    $\Lambda, V \leftarrow sort(\Lambda)$
    $\mathbf{V_{noise}} \leftarrow \mathbf{V_{(m+1):n_s}}$
    $\mathbf{B_{i,j}} \leftarrow \frac{1}{\mathbf{V_{noise}^T V_{noise}}}$
```

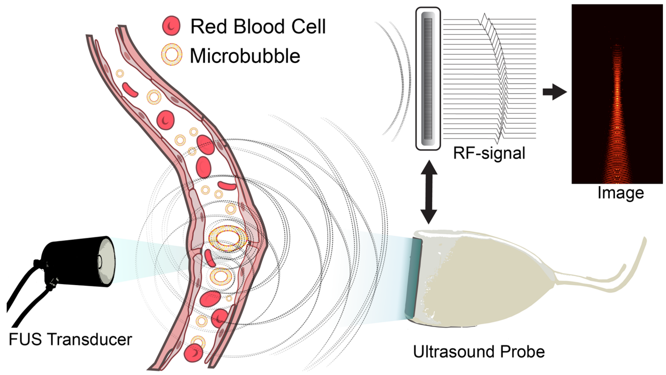

Fig. 1. An illustration of a cavitation imaging setup, with a focused ultrasound generating a signal that cavitates lipid microbubbles in the targeted vasculature. This signal is received by a traditional ultrasound probe in passive listening mode, and beamformed to generate cavitation images.

[32], [33]:

$$x(t) = exp\left(\frac{-|t - t_0 + \phi|}{\theta}\right) \tag{14}$$

Where t_0 represents the time of the cavitation event, ϕ is a stochastic variable representing a small random time shift, and θ, referred to by Vokurka as the "time-condition", controls the width of the cavitation event's build-up and ramp-down. θ can also be manipulated stochastically. The process may be repeated at regular time periods T, corresponding to a FUS pressure cycle's period, and for many point-scatterers:

$$x(t) = \sum_{n=0}^{N_p} \sum_{b=0}^{N_b} exp\left(\frac{-|t - nT - \phi_{n,b}|}{\theta_{n,b}}\right) \tag{15}$$

Where N_p is the number of periods, and N_b is the number of scatterers. To model the RF data received at a transducer's location, $x(t)$ is delayed by the propagation time between the scatterer's location and the transducer, and scaled by $\frac{1}{r}$ to account for proportional spherical spreading. Additionally, a bandpass filter is applied to mimic the frequency response of an imaging probe. The virtual probe used in this work consists of a 64-element 82 mm linear array with a center frequency of 3.21 MHz, a pitch of 1.28 mm, and a pass-band of 1.2 to 5.2MHz. Image reconstruction was performed for a 128 × 128 pixel grid using a 1000 time-point integration window sampled at 12.8 MHz.

Experimental Methods and Materials: To validate the computational results and evaluate beamformer performance for cavitation mapping, two in vitro models were used. In both models, in-house lipid microbubbles were diluted and infused through tubing using a 3 mL syringe with an 18-gauge tip. The microbubbles were prepared using DSPC and DSPE-PEG2000 at a 2.53:1 weight ratio, with perfluoropropane as the gas core. The resulting bubbles are polydisperse ranging from 200 nm to 10 μm in diameter, with the majority measuring $1 - 2\mu m$. The concentration was approximately 5×10^9 bubbles per mL. For imaging, the bubbles are diluted 1:1000 in phosphate buffered saline (PBS) solution.

In the double tube phantom setup (Fig. S4), two 1 mm inner-diameter PTFE tubes (McMaster-Carr, Princeton, NJ, USA) were positioned in the focal region of a 500-kHz FUS transducer (FUS Instruments, Toronto, ON, Canada). The tubes were spaced apart axially to the FUS focal direction by 5 mm so that the bottom tube was in the center of the focus at 24.5 mm, and the top tube at 29.45 mm. Additionally, the top tube was spaced apart laterally by 2.3 mm so that the expected pressure at the far-tube was approximately 0.3 times the pressure amplitude in the center of the focus. Cavitation was induced using a peak rarefactional pressure of 1.5 MPa in the focus for the near-tube, corresponding to 0.45 MPa in the far-tube, with a pulse length of 10 ms and a repetition frequency of 10 Hz. An L12-5 38 mm imaging probe (Philips/ATL, Cambridge, MA, USA) was aligned along the radial axis of the FUS focus, at 25 mm from the far tube. This probe was selected to analyze the high harmonics and ultraharmonics of the incoming signal while also providing an adequate frequency range for higher resolution B-Mode images. The probe was used to transmit a basic B-mode flash sequence for localization, followed by passive RF data acquisition for cavitation imaging. Both B-mode and passive cavitation images were captured using a Verasonics Vantage 256 system (Verasonics, Kirkland, WA, USA) sampled at 33.25 MHz and beamformed on a Dell Precision workstation (Dell Inc., Round Rock, TX, USA) equipped with an Intel Xeon W-2255 processor (Intel, Santa Clara, CA, USA). Inertial cavitation activity was confirmed in the near-tube region, while stable cavitation behavior was observed in the far-tube, as assessed by passive cavitation detection.

To test the robustness of each beamformer with a skull phantom, a rat skull was positioned in water at 25 mm below the FUS transducer (Fig. S8). The L12-5 probe was placed at a 90-degree angle to the FUS focal axis, aligned parallel to the anterior–posterior axis of the skull. The skull was rotated 45 degrees

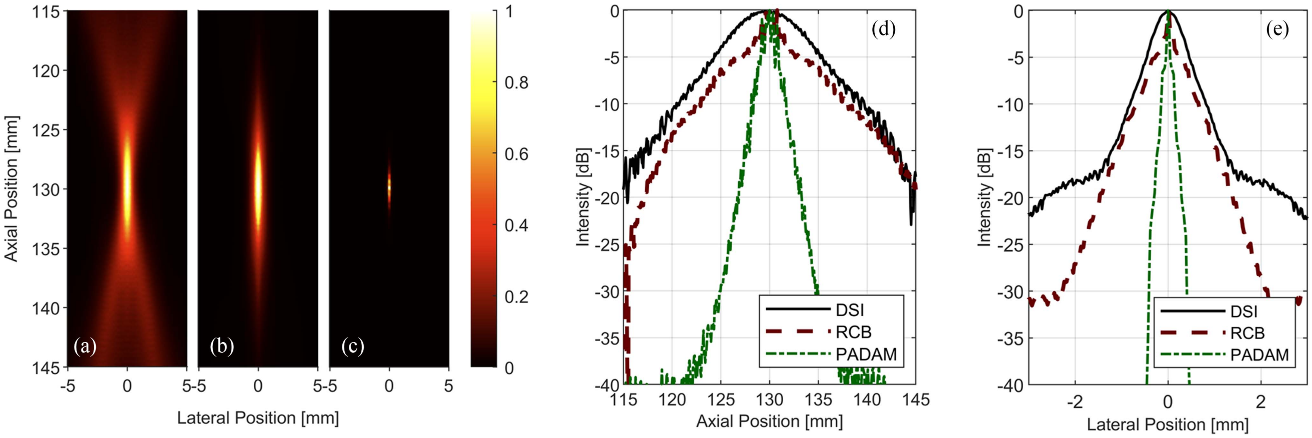

Fig. 2. In-silico passive cavitation images were generated using the Vokurka model and beamformed with: (a) Delay-Sum-Integrate (DSI), (b) the Robust Capon Beamformer (RCB), and (c) PADAM with $m = 1$. Each image is normalized between 0 and 1, with pixel intensities representing pseudo-power. Panels D and E depict the corresponding axial and lateral beamwidth profiles, respectively, for each beamformer using a linear array at a point-source depth of 130 mm.

toward the L12-5 probe to ensure that both the FUS beam and resulting cavitation emissions passed through the parietal bone. A 1.2 mm hole was drilled in the eye cavity of the frontal bone, and a 1 mm inner-diameter PTFE tube was threaded through the cranial cavity. Cavitation was induced using 500-kHz FUS at a peak negative pressure of 1.5 MPa for 10 seconds, with 10 ms pulse durations and a pulse repetition frequency of 10 Hz. The same Verasonics system was used to acquire RF-Data and generate B-mode localization images, sampled at 33.25 MHz. Cavitation image reconstruction was performed on a 128×128 pixel grid using a 2048 time-point integration.

Comparison Metrics: To effectively compare the performance of the beamformers, several metrics were used. The point spread function (PSF) of a beamformer is the ideal metric, although it is spatially dependent: every pixel exhibits a slightly different point-spread (Fig. S1). For this work, the full-width at half-maximum (FWHM) was used as the measure of beam profile width in both the axial and lateral directions.

The mean-square intensity (MSI) of the pixels serves as a measure of the amount of relative noise or cumulative artifact presence in an image. This metric encompasses both signal and artifacts; however, since the size of cavitating microbubbles is on the micrometer scale, an order of magnitude smaller than the millimeter scale used in ultrasound imaging applications, the cavitation source is point-like and much smaller than a single pixel. For the images generated in this work, a single, stationary cavitation source (such as those simulated by Vokurka's model) would produce minimal signal intensity, while the overwhelming majority of observed pixel intensity comes from artifacts and the point-spread function. The beamformers used in this work are not energy-preserving, so MSI can be used to quantify artifacts and the effects of point-spread. It is calculated by:

$$MSI = \frac{1}{N_x N_y} \sum_{i=0}^{N_x} \sum_{j=0}^{N_y} P_{i,j}^2 \tag{16}$$

TABLE I
BEAM WIDTHS (MM)

	DSI		RCB		PADAM	
	Axial	Lateral	Axial	Lateral	Axial	Lateral
-3 dB	8.1	0.696	2.58	0.216	1.02	0.072
-6 dB	12.54	1.08	9.36	0.744	1.98	0.12
-10 dB	18.9	1.608	15.06	1.32	3.42	0.312

Where N_x, N_y are the dimensions of the image in pixels, and P_{ij} is the pseudo-intensity at pixel i, j. This work uses MSI to approximate the amount of noise in a beamformed image, comparing beamformers for differently sized bubble clusters.

III. RESULTS

Localization and Speed: To compare PADAM to RCB and DSI, the Vokurka model was used with a single cavitation source positioned axially at 40 mm and centered laterally in a virtual probe's field of view. The images were beamformed, and the output images were normalized on a linear scale for comparison, as PADAM is not a power-based beamformer and the intensity of the images cannot be compared directly (Fig. 2). PADAM exhibits a point-like source stretched by the axial resolution of the system, without a tail artifact, whereas RCB displays a much larger area without a tail, and DSI shows the classical X-shaped tail artifact. The axial and lateral beamwidths for each beamformer are also shown in Fig. 2 and summarized in Table I, with PADAM demonstrating a significantly narrower width.

To evaluate computational performance, beamforming was performed in MATLAB on a 100×100 pixel image with 2,000 timepoints using an Intel i9-13900K CPU. The average computation times were 2.15 seconds for DSI, 6.33 seconds for RCB, and 5.69 seconds for PADAM. However, PADAM offers a significant advantage over RCB when testing multiple parameters: the eigenvalue decomposition can be re-used for each parameter desired and simply indexed, whereas RCB must employ both

TABLE II
PARAMETER BEAMFORMING TIMES (SECONDS)

	RCB (ε)	PADAM (m)
1 parameter	6.33	5.69
20 parameters	22.04	8.52
50 parameters	43.41	13.5

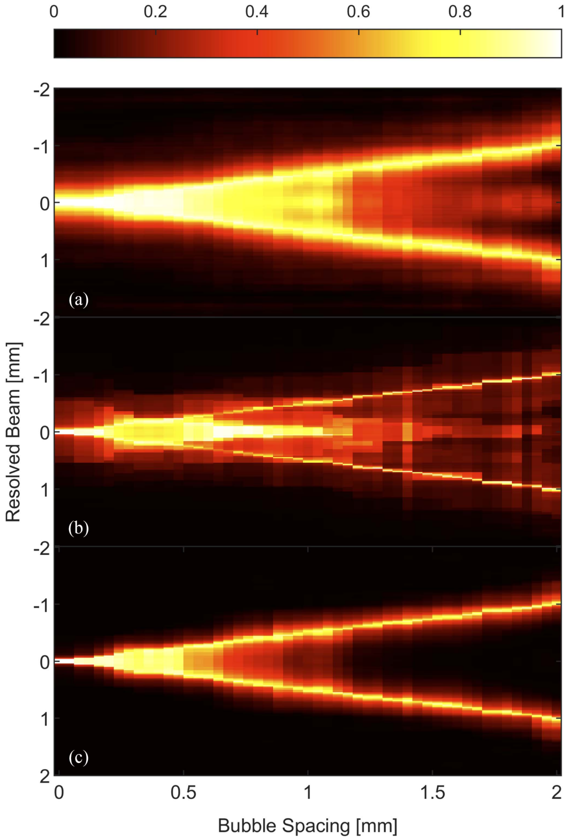

Fig. 3. Point-source resolvability, where (a) is DSI, (b) shows RCB, and (c) depicts PADAM with $m = 1$. Each column of the panels is a lateral line-image taken at the focus-depth of two point sources which step away from each other from left to right.

the Lagrange multiplier and Newton's methods to re-solve the optimization problem for a new ε. The times for beamforming a set of images for several numbers of parameters is listed in Table II.

The Vokurka model was further used to quantify resolvability, as illustrated in Fig. 3. Two bubble sources, initially co-located, were incrementally separated laterally, and a one-dimensional lateral profile was extracted at the depth of the sources for each separation distance. These line-images were concatenated to visualize how resolution changes with increasing source separation. (Note: in Fig. 3, each line-image was individually normalized from 0 to 1 to highlight relative contrast.) To mitigate stochastic variability inherent in the Vokurka model, 30 line-images were averaged at each spacing. As shown in Fig. 3, while the RCB beamformer appears to produce sharper profiles at larger separations, it exhibits a persistent central artifact even when sources are well resolved. A similar artifact is observed with DSI. Using the definition of resolution as the minimum distance at which two point sources remain distinguishable, the observed resolutions are approximately 1 mm for DSI, 0.65 mm for RCB, and 0.5 mm for PADAM based on a visual estimate. These results highlight PADAM's improved spatial discrimination, particularly in closely spaced cavitation scenarios.

To simulate a bubble cloud within the therapeutic focal region, Vokurka-modeled bubbles were randomly distributed within an ellipsoidal volume approximating the FUS focal zone. These clustered bubble distributions serve as ideal test cases for evaluating artifact removal, as tail artifacts between adjacent bubbles can overlap and create misleading signals in regions devoid of actual bubbles. As seen in Fig. 4, PADAM demonstrates significantly lower MSI values compared to DSI and RCB, highlighting its superior performance in cavitation localization and tail artifact suppression. Despite a thorough parameter sweep aimed at optimizing RCB performance, it consistently underperformed relative to PADAM. The elliptical output patterns commonly observed in RCB reconstructions appear to stem from the fixed ε coefficient, which may artificially constrain the steering vector and limit spatial accuracy. These findings suggest that PADAM is highly effective at reducing noise and enhancing spatial localization in scenarios involving clustered cavitation.

The PADAM Parameter m: As outlined in Section II, PADAM operates by assuming a number of sources m, from which the signal and noise subspaces are determined using accepted and rejected eigenvectors. This means that at each pixel, only the eigenvectors corresponding to the m largest eigenvalues are included. The largest m eigenvectors correspond to the most correlated sources in the spatial covariance matrix at that pixel, effectively filtering out uncorrelated signals. Additional eigenvalues in the spatial covariance matrix may represent "weaker" sources at other locations with lower correlation, while near-zero eigenvalues primarily correspond to noise. It turns out that the exact number of nonzero eigenvalues present in a signal's spatial covariance matrix is 2 times the number of frequencies in that signal [34].

In this line of logic, increasing m to larger integers may introduce a leakage signal from other sources, as well as potential noise. Fig. 5 displays a further confirmation of this concept, where a PADAM image is beamformed with a sine-wave source with amplitude of 1 MPa and frequency $f = 3.21$ MHz on the left, and a Vokurka source with a mean peak amplitude of 1 MPa on the right. Fig. 5(f) also shows the Vokurka source's eigenvalue pattern, which has 16 eigenvalues that represent the 8 in-band harmonics of the drive frequency, which was 500 KHz, seen in D).

Sinewave signals generate a spatial covariance matrix that has exactly two non-zero eigenvalues, which are strong compared to the many non-zero eigenvalues of the Vokurka source, seen in Fig. 5(f)). At $m = 2$, only the sine-wave is visible in the entire image, as it is highly correlated and dominates the signal, even at the Vokurka source's pixel location. However, at $m = 3$, more eigenvalues are included than the sine-wave's alone, allowing one from the Vokurka source. The Vokurka source appears at approximately half the intensity of the sinewave source, since two eigenvectors belong to the sinewave and only one from

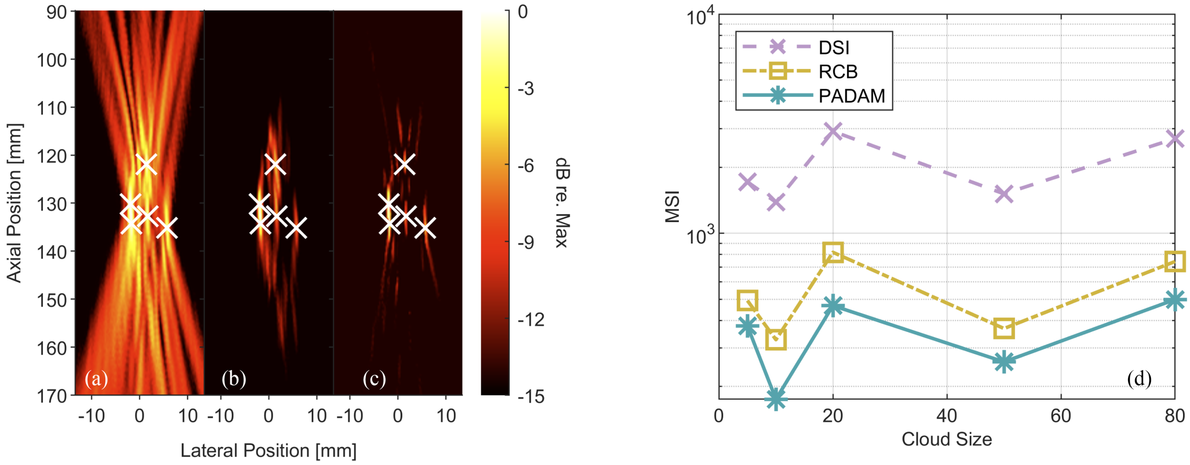

Fig. 4. Representative cavitation images from a 5-source simulation using each beamforming method. The true source locations are overlaid as white x's. (a) depicts DSI, (b) RCB, and (c) PADAM $m = 3$. The mean-square intensity (MSI) shown in (d) depicts the artifact reduction ability for each beamformer across four bubble cluster sizes: 10, 20, 50, and 80.

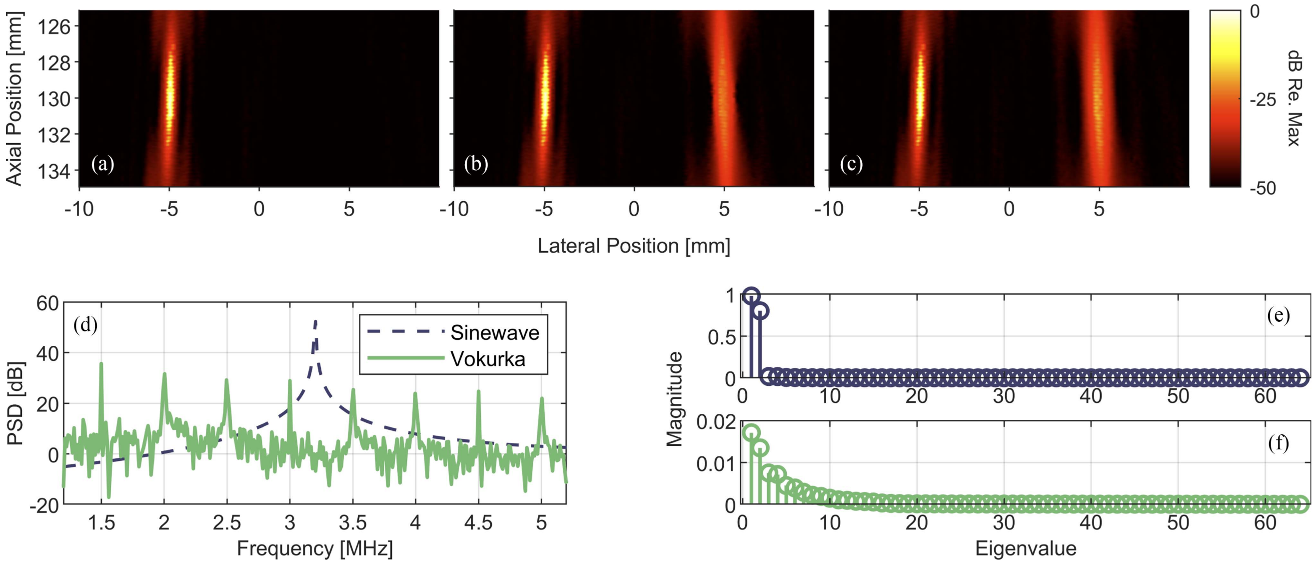

Fig. 5. PADAM Frequency Component Separation Test Using a Pure Tone and a Vokurka Source. (a)–(c) display PADAM beamformed images from RF data containing two sources: a pure sine wave (3.21 MHz, 1 MPa) positioned on the left, and a Vokurka-modeled source with a mean peak amplitude of 1 MPa positioned on the right. Beamforming was performed with PADAM using (a) $m = 2$, (b) $m = 3$, and (c) $m = 4$. (d) shows frequency spectra of the sinewave and the Vokurka source. (e) shows the eigenvalue distribution at the first pixel for the pure sine wave, and (f) shows the eigenvalue distribution for the Vokurka source.

the Vokurka source. At $m = 4$, both regions appear similar in intensity. Beyond $m = 4$, more eigenvectors correspond to the Vokurka source, which shift the visual weight towards the right. Notably, the eigenvectors in PADAM are not scaled by their eigenvalues, leading to a stacking effect. Admitting too many sources can result in overlaying eigenvectors from closely located sources, causing 2 - 3 pixels to dominate the image for a single source. This can misidentify the strongest source's location due to factors like the tail artifact, if m is set too high.

To further illustrate PADAM's ability to distinguish cavitation types, a synthetic frequency component separation test was performed using Vokurka-modeled sources (Fig. 6). Five sources were arranged in a rectangular configuration, with one located at the center. The time-conditioning parameter ("θ") was increased for the center, resulting in longer pulse widths and a different harmonic-to-inharmonic energy ratio, serving as a proxy for stable cavitation, while the outer source with low θ modeled inertial cavitation. Fig. 6 displays PADAM reconstructions for $m = 1, 8, 20$, showing that the contrast of the central inertial source increases with m. It should be noted that Fig. 6(a)–(c) are normalized, and that the contrast of the outer sources slightly increase as seen in Fig. 6(d)), but this change is overshadowed by the center source. Fig. 6(e)) illustrates the corresponding frequency spectra: the three dominant peaks are associated with the inertial sources, while the remaining peaks correspond to the stable source. Consequently, the leading eigenvalues in the image primarily originate from the inertial sources until

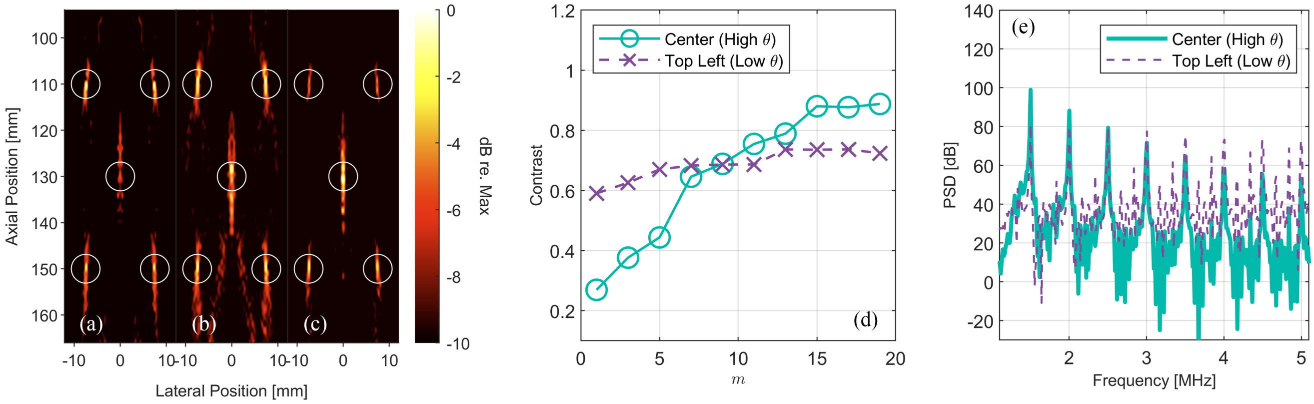

Fig. 6. PADAM Frequency Component Separation Using Synthetic Inertial and Stable Cavitation Sources (Vokurka Model). (a)–(c) show normalized PADAM-reconstructed images using $m = 1$, 8, and 20, respectively. The simulation includes a central synthetic stable cavitation source and four inertial cavitation sources located near the corners, all with equal peak pressures. For results using unequal source amplitudes, refer to Fig. S2 and Fig. S3. At low m, the stable cavitation signal is suppressed due to the dominant low-frequency components from the inertial sources, as reflected in the contrast values (d) and frequency spectra (e). The strongest spectral peaks in E originate from the peripheral inertial sources. At higher values of m (8 and 20), the stable cavitation source's higher-frequency components are incorporated via eigen-decomposition, resulting in increased contrast in the reconstructed image. Contrast was calculated as $\frac{I_{\max}-I_{\min}}{I_{\max}+I_{\min}}$.

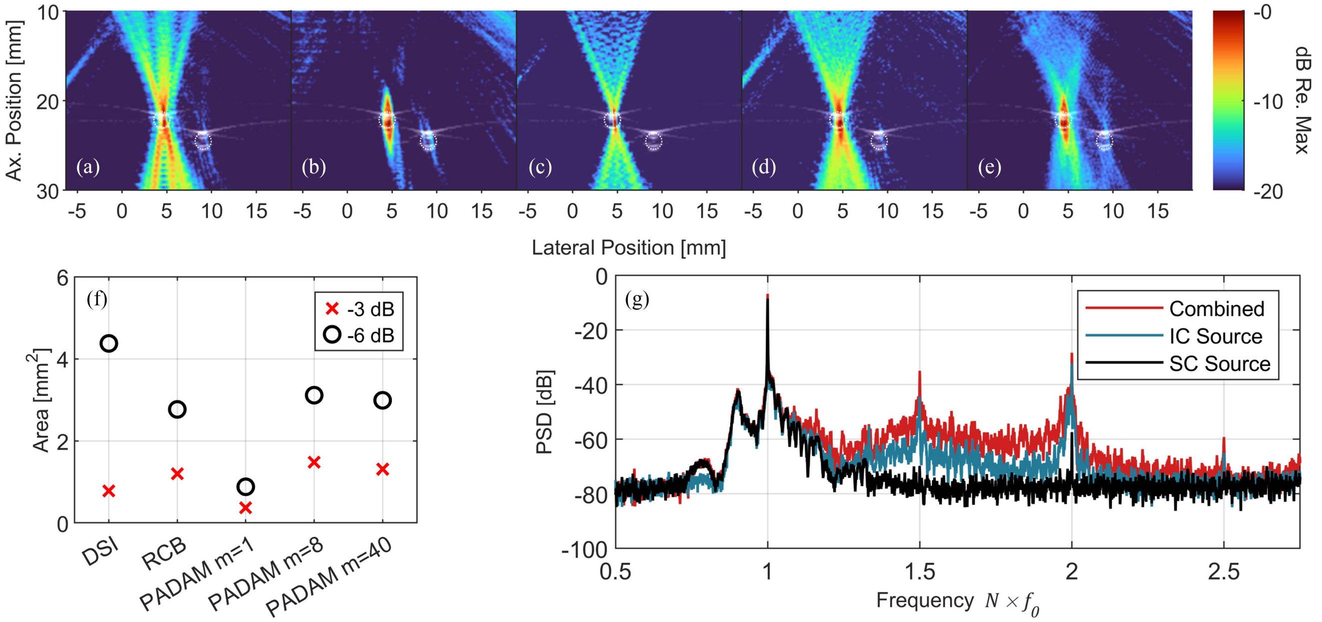

Fig. 7. PADAM Cavitation Classification Test Using a Double-Tube In Vitro Phantom. (a) and (b) show images beamformed using DSI and RCB, respectively, overlaid on a B-mode image for localization. The cross-sections of tubes are visible in the B-mode images, with their perimeters marked by dotted white circles. (c)–(e) display PADAM-reconstructed images using $m = 1$, 8, and 40, respectively. At a FUS target pressure of 1.5 MPa, PADAM reveals inertial cavitation in the left tube and stable cavitation in the right tube, which becomes distinguishable when m reaches 8 and above. Inertial and stable cavitation behaviors were confirmed by passive cavitation detection, as shown in (g). (f) highlights the -3 and -6 dB regions of the main lobe, demonstrating the strongest localization achieved with PADAM at $m = 1$.

$m = 8$ and 9, where contributions from the stable source begins to emerge. The contrast of the sources as shown in Fig. 6(d) highlights this effect. This finding suggests that PADAM may enable differentiation between stable and inertial cavitation within an image, a capability further explored in the in vitro experiments described below.

In Vitro Models: To test if PADAM could provide superior artifact reduction and harmonic differentiation in-vitro as seen in the computational models, we first performed an in vitro experiment in a double-tube phantom. Fig. 7 shows cavitation images beamformed with DSI and RCB ($\varepsilon = 10$) for comparison, and PADAM images with $m = 1$, 8, and 40. Compared to RCB and DSI, PADAM correctly isolates the inertial cavitation to the near-tube at low m, and also reveals the stable cavitation in the far-tube at higher m values starting at $m = 8$. This effect is further seen when more frequency components are included at $m = 40$. This provides evidence that PADAM can isolate inertial cavitation regions from stable ones by selecting low m, and that increasing m can find stable cavitation even if it is at a much lower pressure amplitude.

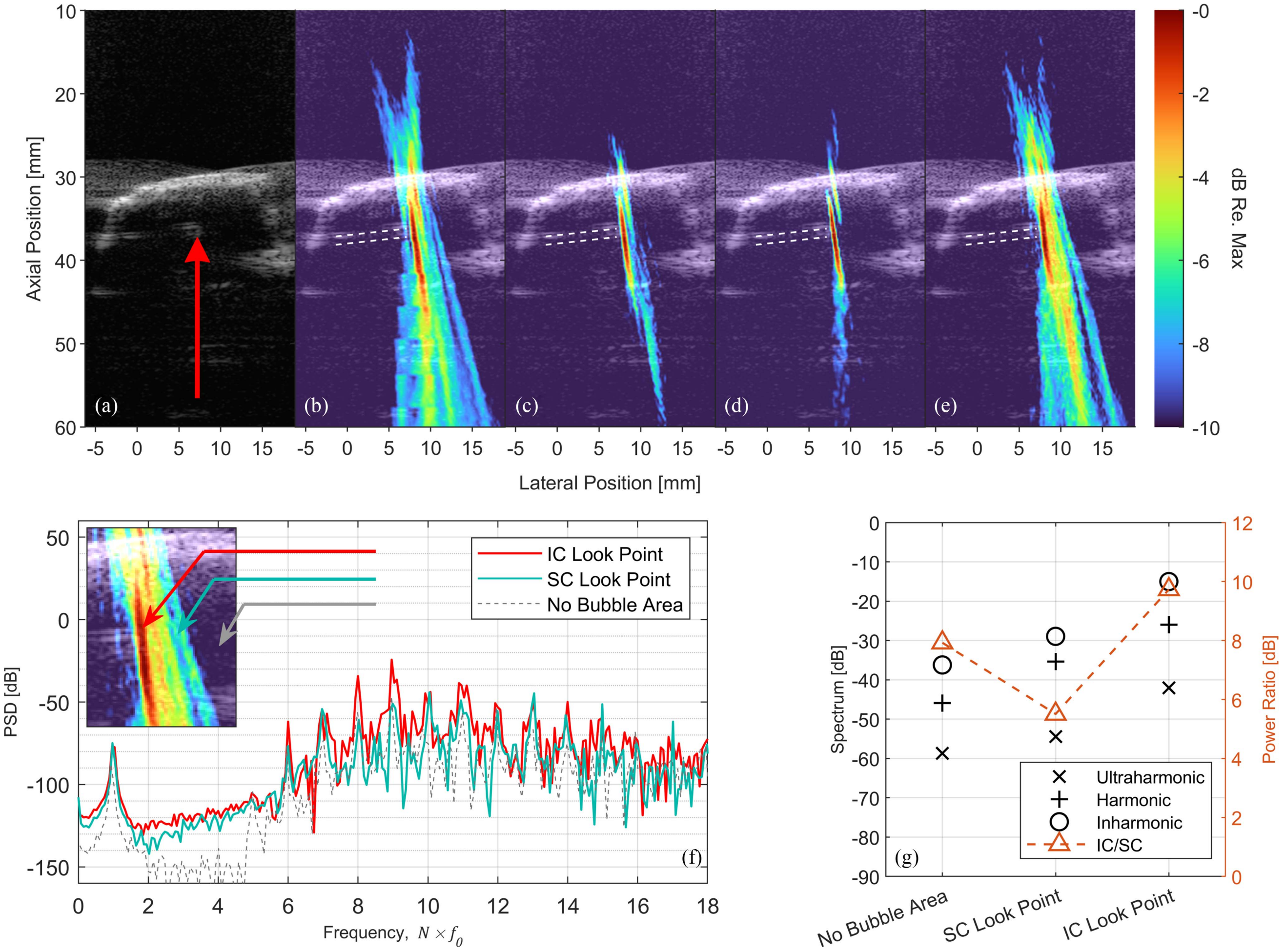

Fig. 8. PADAM Robustness Test Using a Rat Skull Phantom. The rat skull is visible in white at a depth of 29 mm, and the embedded tube at 35 mm is marked by a red arrow in the B-mode image in (a). (b)–(e) show the same frame of RF data beamformed using (b) DSI, (c) RCB, (d) PADAM with $m = 1$, and E) PADAM with $m = 10$. PADAM demonstrates superior localization and clear improvement over RCB, particularly in isolating the off-target cavitation lobe observed near (8, 30) mm at the skull base in (d). (f) displays the frequency spectra of the RF data at three look points (delayed and averaged across elements), as indicated by the arrows in the zoomed subpanel of (e). (g) quantifies the harmonic, ultraharmonic, and inharmonic components, confirming that stable cavitation (SC) versus inertial cavitation (IC) can be dynamically distinguished in PADAM images, as indicated by the IC/SC ratio.

To further evaluate PADAM's performance in the presence of skull-induced aberration, cavitation images from the in vitro skull model are shown in Fig. 8(g). All three beamformers localized the cavitation source near the true position of the tube observed in B-mode imaging. PADAM demonstrated markedly improved localization compared to DSI, particularly at low values of m . RCB was able to effectively suppress most of the tail artifacts; however, PADAM was more effective, allowing for easier identification of an off-target cavitation source at the skull base (30.5 mm axially) in addition to the microbubble cavitation in the tube (at 36.6 mm). Increasing m to 10 widens the image lobes, suggesting stable cavitation to the right of the focus, seen in Fig. 8(e). We investigated this hypothesis by selecting three look-points from 1) the main lobe of the image, 2) a side-lobe area, and 3) the periphery with no bubbles as a control. We calculated the beamformed frequency spectrum by applying delay-and-sum across the channels for the time RF-data delayed for each location and taking the Fourier Transform, seen in Fig. 8(f). We lastly isolated the harmonic, inharmonic, and broadband components of this spectrum, and calculated the ratio of inertial-cavitation to stable cavitation power as

$$R_{IC/SC} = \frac{\sum E_{broadband}}{\sum E_{ultra} + \sum E_{harm}} \tag{17}$$

in Fig. 8(g), which shows a low IC/SC ratio for the stable look-point and high ratio for the IC look-point, confirming that mostly stable cavitation occurs at the right-lobe look point. This suggests PADAM can localize stable cavitation when comparing to a low m image in the presence of the skull barrier and with aberration effects by increasing m, which suggests that this beamformer will perform classification well in-vivo.

IV. DISCUSSION

Our results demonstrate that PADAM in the time domain is a highly effective approach for passive cavitation localization. PADAM consistently outperformed DSI and RCB in both lateral and axial resolution, as well as point-spread function size for the observed areas in the imaging plane. Furthermore, PADAM exhibited superior tail and reflection artifact reduction compared to RCB for both singular sources and clusters, both in-silico and in-vitro, with and without a skull.

A key advantage of PADAM lies in its parameter m, which reflects the frequency richness of incoming signals. Although PADAM operates in the time domain, this parameter enables spatial filtering based on frequency content. As a result, PADAM offers a physically meaningful and intuitive avenue to distinguish between different frequency spectra and, consequently, between cavitation mechanisms.

As discussed in the Introduction, stable and inertial cavitation induce distinct bio-effects: stable cavitation facilitates targeted vascular permeation, whereas inertial cavitation enables tissue ablation. By adjusting m, users can localize sources or clusters (i.e., setting m to 1) to find inertial-like cavitation sources,or increase m to visualize stable cavitation regions as long as ultraharmonics are present. PADAM's ability to dynamically distinguish cavitation mechanisms has significant implications in image-guided FUS therapy, particularly for applications requiring selective monitoring of stable versus inertial cavitation. This is crucial when avoiding unintended bio-effects from inertially cavitating bubbles in sensitive areas or in off-target zones frequency seen in-vivo.

Compared to RCB, PADAM is easier to use and more computationally efficient. Unlike RCB, which requires parameter tuning (i.e., ε) to optimize performance, often resulting in inconsistent image quality, PADAM does not require parameter searches, making it more user-friendly. Additionally, PADAM is computationally faster than RCB, as it relies on eigenvalue decompositions rather than matrix inversions for each pixel. Furthermore, the algorithm's flexible handling of signal and noise subspaces allows for rapid computation of multiple images with varying m values, rather than rerunning the algorithm separately for each case. A typical scenario of selecting the parameter m involves selecting 10–15 test values ranging from low (1) to high (40), and noting at which m the cavitation footprint expands significantly, revealing quieter sources with wider frequency-spectra. PADAM is also a candidate for parallelization and speedup by using algorithms that identify the largest several eigenvalues (namely, the power method) instead of every eigenvalue.

However, a key limitation of PADAM is that it is not a power-based beamformer, and should not be used by itself to monitor cumulative energy absorption. As discussed in Section II, PADAM assigns pixel values inversely proportional to noise correlation, essentially measuring what is not noise. Future work could explore using PADAM images as masks over a power-based beamformer to generate comprehensive dosage maps. Additionally, PADAM currently requires manual selection of the parameter m; future work will focus on developing data-driven or biologically informed strategies for adaptive selection of this parameter. Third, while other methods such as Delay-Multiply-and-Sum (DMAS) and sparse reconstruction are relevant in broader ultrasound contexts, they were not directly compared here. DMAS offers limited resolution improvements in PCI (compared to DSI) and has not seen widespread adoption, while sparse reconstruction is more applicable to compressed sensing or accelerated imaging—beyond the scope of the current fully sampled study. Nevertheless, these methods hold promise for extending PADAM's capabilities, and we plan to explore them in future works aimed at real-time or resource-constrained applications. Lastly, extending PADAM to the frequency domain would enable direct frequency selection as it does with DSI, allowing for isolation of the ultraharmonic and harmonic bands associated with stable cavitation.

There were also several experimental limitations in both the in-silico and in-vitro methods. The Vokurka model, while useful, assumes a smooth ramp-down of the impulse pressure, which oversimplifies actual cavitation behavior. This study also varied the Vokurka θ time-condition parameter to mimic bubble dynamics. While altering θ modified the frequency spectrum and the ratio of harmonic to inharmonic energy, it did not generate the ultraharmonics commonly observed in cavitation behavior. In addition, the inharmonic content in the Vokurka model mainly arises from aliasing rather than a well-defined inertial cavitation mechanism, limiting its ability to fully replicate stable and inertial cavitation. However, the fundamental principle underlying PADAM, differentiating sources dynamically based on frequency content, remains effectively demonstrated and was further validated by the in-vitro results.

In the phantom studies, the double-tube experimental setup was designed to capture both inertial cavitation in the near-tube and stable cavitation far-tube simultaneously. Future studies could investigate at lower concentrations to track individual bubble dynamics over time as they migrate into a FUS focal region. Another limitation of the current in vitro study was the skull model thickness. PADAM performed well in the presence of a thin rat skull at a low drive frequency, showing little focal aberration consistently with the other beamformers. However, higher-frequency components such as harmonics and ultraharmonics above 2 MHz will have wavelengths comparable to skull thickness, and thus may experience greater distortion. Future studies should examine PADAM's performance through thicker and more acoustically complex barriers, such as primate skulls. In vivo studies will also be critical for assessing PADAM's ability to differentiate cavitation regimes in a more realistic biological environment. While PADAM does not compensate for skull-induced focal shifts, our results suggest it remains robust in the presence of absorption, noise, and structural inhomogeneities—conditions that often degrade performance in conventional beamformers.

V. CONCLUSION

This work introduces PADAM as a time-domain PCI method and compares its performance to established beamformers such as DSI and RCB. Our findings show that PADAM offers enhanced resolution, robust artifact suppression, and a physically interpretable and intuitive input parameter that can isolate stable and inertial cavitation. PADAM also achieves improved computational efficiency over RCB by eliminating the need for per-pixel matrix inversions. Most notably, PADAM's ability to differentiate cavitation mechanisms through its parameter m represents a meaningful advancement in PCI. This dual capability, not only localizing cavitation but also characterizing its nature dynamically, holds significant promise for guiding and controlling ultrasound therapies.

ACKNOWLEDGMENT

The content is solely the responsibility of the authors and does not necessarily represent the official views of the NIH. A provisional patent application (63/783,884) has been filed for the imaging algorithm described herein to support future commercial or clinical translation.

REFERENCES

[1] J. K. Khalsa et al., "Immune phenotyping of diverse syngeneic murine brain tumors identifies immunologically distinct types," *Nature Commun.*, vol. 11, no. 1, Aug. 2020, Art. no. 3912.
[2] C. D. Arvanitis, G. B. Ferraro, and R. K. Jain, "The blood–brain barrier and blood–tumour barrier in brain tumours and metastases," *Nature Rev. Cancer*, vol. 20, no. 1, pp. 26–41, Jan. 2020.
[3] W. M. Zhu et al., "Neurovascular coupling mechanisms in health and neurovascular uncoupling in alzheimer's disease," *Brain, A J. Neurol.*, vol. 145, no. 7, pp. 2276–2292, Jul. 2022.
[4] C. T. Curley et al., "Focused ultrasound immunotherapy for central nervous system pathologies: Challenges and opportunities," *Theranostics*, vol. 7, no. 15, pp. 3608–3623, Aug. 2017.
[5] J. B. Joiner, Y. Pylayeva-Gupta, and P. A. Dayton, "Focused ultrasound for immunomodulation of the tumor microenvironment," *J. Immunol.*, vol. 205, no. 9, pp. 2327–2341, Nov. 2020.
[6] S. Chen et al., "A review of bioeffects induced by focused ultrasound combined with microbubbles on the neurovascular unit," *J. Cereb. Blood Flow Metab.*, vol. 42, no. 1, pp. 3–26, Jan. 2022.
[7] V. Krishna et al., "Trial of globus pallidus focused ultrasound ablation in Parkinson's disease," *New England J. Med.*, vol. 388, no. 8, pp. 683–693, Feb. 2023.
[8] P. C. Lyon et al., "Safety and feasibility of ultrasound-triggered targeted drug delivery of doxorubicin from thermosensitive liposomes in liver tumours (TARDOX): A single-centre, open-label, phase 1 trial," *Lancet Oncol.*, vol. 19, no. 8, pp. 1027–1039, Aug. 2018.
[9] A. R. Rezai et al., "Ultrasound blood–brain barrier opening and aducanumab in Alzheimer's disease," *New England J. Med.*, vol. 390, no. 1, pp. 55–62, Jan. 2024.
[10] S. M. Thompson et al., "Heat stress induced cell death mechanisms in hepatocytes and hepatocellular carcinoma: In vitro and in vivo study," *Lasers Surg. Med.*, vol. 46, no. 4, pp. 290–301, Apr. 2014.
[11] T. Sun et al., "Closed-loop control of targeted ultrasound drug delivery across the blood–brain/tumor barriers in a rat glioma model," *Proc. Nat. Acad. Sci.*, vol. 114, no. 48, pp. E10281–E10290, Nov. 2017.
[12] N. McDannold et al., "Acoustic feedback enables safe and reliable carboplatin delivery across the blood-brain barrier with a clinical focused ultrasound system and improves survival in a rat glioma model," *Theranostics*, vol. 9, no. 21, pp. 6284–6299, Aug. 2019.
[13] C. D. Arvanitis and N. McDannold, "Integrated ultrasound and magnetic resonance imaging for simultaneous temperature and cavitation monitoring during focused ultrasound therapies," *Med. Phys.*, vol. 40, no. 11, 2013, Art. no. 112901.
[14] C. Coviello et al., "Passive acoustic mapping utilizing optimal beamforming in ultrasound therapy monitoring," *J. Acoust. Soc. Amer.*, vol. 137, no. 5, pp. 2573–2585, May 2015.
[15] M. Gyongy et al., "Use of passive arrays for characterization and mapping of cavitation activity during HIFU exposure," in *Proc. 2008 IEEE Ultrasonics Symp.*, Nov. 2008, pp. 871–874.
[16] K. J. Haworth et al., "Using passive cavitation images to classify high-intensity focused ultrasound lesions," *Ultrasound Med. Biol.*, vol. 41, no. 9, Jun. 2015, Art. no. 2420.
[17] M. Gyongy and C. -C. Coussios, "Passive spatial mapping of inertial cavitation during HIFU exposure," *IEEE Trans. Biomed. Eng.*, vol. 57, no. 1, pp. 48–56, Jan. 2010.
[18] C. H. Farny, R. G. Holt, and R. A. Roy, "Temporal and spatial detection of HIFU-induced inertial and hot-vapor cavitation with a diagnostic ultrasound system," *Ultrasound Med. Biol.*, vol. 35, no. 4, pp. 603–615, Apr. 2009.
[19] K. J. Haworth et al., "Passive cavitation imaging artifact reduction using data-adaptive spatial filtering," *IEEE Trans. Ultrason., Ferroelectr., Freq. Control*, vol. 70, no. 6, pp. 498–509, Jun. 2023.
[20] V. Perrot et al., "So you think you can DAS? A viewpoint on delay-and-sum beamforming," *Ultrasonics*, vol. 111, Mar. 2021, Art. no. 106309.
[21] S. J. Norton and I. J. Won, "Time exposure acoustics," *IEEE Trans. Geosci. Remote Sens.*, vol. 38, no. 3, pp. 1337–1343, May 2000.
[22] K. J. Haworth et al., "Quantitative frequency-domain passive cavitation imaging," *IEEE Trans. Ultrason., Ferroelectr., Freq. Control*, vol. 64, no. 1, pp. 177–191, Jan. 2017.
[23] S. Bae et al., "Real-time passive acoustic mapping with enhanced spatial resolution in neuronavigation-guided focused ultrasound for blood-brain barrier opening," *IEEE Trans. Biomed. Eng.*, vol. 70, no. 10, pp. 2874–2885, Oct. 2023.
[24] H. A. S. Kamimura et al., "Real-time passive acoustic mapping using sparse matrix multiplication," *IEEE Trans. Ultrason., Ferroelectr., Freq. Control*, vol. 68, no. 1, pp. 164–177, Jan. 2021.
[25] E. Lyka et al., "Passive acoustic mapping using data-adaptive beamforming based on higher order statistics," *IEEE Trans. Med. Imag.*, vol. 37, no. 12, pp. 2582–2592, Dec. 2018.
[26] R. M. Jones, D. McMahon, and K. Hynynen, "Ultrafast three-dimensional microbubble imaging in vivo predicts tissue damage volume distributions during nonthermal brain ablation," *Theranostics*, vol. 10, no. 16, pp. 7211–7230, 2020.
[27] J. Li, P. Stoica, and Z. Wang, "On robust Capon beamforming and diagonal loading," *IEEE Trans. Signal Process.*, vol. 51, no. 7, pp. 1702–1715, Jul. 2003.
[28] S. Lu et al., "Passive acoustic mapping of cavitation using eigenspace-based robust capon beamformer in ultrasound therapy," *Ultrasonics Sonochemistry*, vol. 41, pp. 670–679, Mar. 2018.
[29] R. Schmidt, "Multiple emitter location and signal parameter estimation," *IEEE Trans. Antennas Propag.*, vol. TAP-34, no. 3, pp. 276–280, Mar. 1986.
[30] M. Polichetti et al., "Use of the cross-spectral density matrix for enhanced passive ultrasound imaging of cavitation," *IEEE Trans. Ultrason., Ferroelectr., Freq. Control*, vol. 68, no. 4, pp. 910–925, Apr. 2021.
[31] K. Vokurka, "A simple model of a vapor bubble," *J. Acoust. Soc. Amer.*, vol. 81, no. 1, pp. 58–61, Jan. 1987.
[32] S. Buogo and K. Vokurka, "Intensity of oscillation of spark-generated bubbles," *J. Sound Vib.*, vol. 329, no. 20, pp. 4266–4278, Sep. 2010.
[33] K. Vokurka, "Cavitation noise modeling and analyzing," in *Proc. CD-ROM Proc. Forum Acousticum*, 2002, vol. 2002.
[34] W. D. Penny, "Signal processing course," 2009. [Online]. Available: https://www.fil.ion.ucl.ac.uk/wpenny/